Materials and Design 105 (2016) 160–170

Contents lists available at ScienceDirect

Materials and Design

journal homepage: www.elsevier.com/locate/matdes

Correlation between porosity and processing parameters in TiAl6V4 produced by selective laser melting

Galina Kasperovich *, Jan Haubrich, Joachim Gussone, Guillermo Requena

Institute of Materials Research, German Aerospace Center (DLR), Germany

ARTICLE INFO

Article history:
Received 1 April 2016
Received in revised form 13 May 2016
Accepted 19 May 2016
Available online 20 May 2016

Keywords:
Selective laser melting
Titanium alloys
Porosity morphology
Synchrotron tomography

ABSTRACT

This study presents the correlation between process parameters and porosity formation in a TiAl6V4 alloy produced by selective laser melting. The porosity is investigated by 2D and 3D methods aiming to identify the mechanisms of void formation, their morphology as well as volume fraction as a function of the energy density. An evident minimum volume fraction is observed between process parameters with significant overheating and insufficient fusion. It is shown that these two marginal regions define two mechanisms of void formation. Two dominant types of voids morphology are identified and examined regarding pore orientation versus their elongation, which together with the curvature distribution analysis allow revealing critical defects.

1. Introduction

Selective laser melting (SLM) is an additive manufacturing technology capable of layer-by-layer fabrication of intricate and net-shaped metallic parts directly from three-dimensional CAD models [1–6]. This renders it very interesting for aerospace industry, where geometrically complex structures of high strength materials are widely used. In particular, the α-β TiAl6V4 (Ti — 6 wt% Al — 4 wt%) alloy is of interest owing to its high specific strength and low density [7].

However, non-optimal process parameters may cause inner defects, e.g. unmolten powder particles, spherical entrapped gas bubbles, cracks and other types of local irregularities [8–9].

Considerable research effort has focused on the influence of process parameters on the microstructure and related mechanical properties of titanium parts produced by SLM. For example, works on SLM of pure Ti [10–12] or Ti-TiB/TiC composite [13–15], TiAl6Nb7 [16], Nitinol [17,18], other β-titanium alloys such as TiNb24Zn4Sn8 [19], novel Ti/Mo composites [4] as well as both TiAl6V4 [20–25] and TiAl6V4-ELI [5,6] alloys have been reported.

Combining different powders and processing the mixture via SLM opens up new consolidation possibilities. Hua et al. [26] combined elemental powder of Ti, Al and V to produce a bulk TiAl6V4 part. Several authors have reported on the production of several types of in-situ metal matrix composites (MMCs), including different titanium matrix composites [27–30]. Vrancken and co-workers [4] investigated a mixture of TiAl6V4-ELI powder with 10 wt% Mo powder. The effect of the power particles shape on the properties of Ti/TiB part was presented by Attar et al. [15].

Various types of defects inherent to the SLM process and their influence on the mechanical properties of the material have been described, e.g. in Refs. [22–25,31]. Thijs et al. [5] discussed the role of scanning parameters (velocity, spot size, scanning strategy etc.) for several standard steels and titanium alloys and investigated qualitatively the types of occurring porosity two-dimensionally (2D). Leuders et al. [32] examined the porosity in SLM manufactured TiAl6V4 three-dimensionally (3D) by X-ray computed tomography. The authors obtained high relative densities ranging from 99.77% up to 100% at a low spatial resolution, i.e. 22 μm pro voxel, which may underestimate the actual porosity volume fraction. Gong et al. [24,33] proposed a classification for the SLM process window. Depending on laser power and scan rate, different process zones were identified corresponding to an incomplete melting, fully dense material, "over-melting" and overheating. The porosity was evaluated statistically using descriptors such as circularity, convexity and elongation and related [34] to the different zones within the process window. Thus, numerous studies focusing on the need of minimization of inherent defects of TiAl6V4 fabricated by SLM are available, but systematic optimizations of the technological process parameters are not sufficiently represented, especially in terms of detailed quantitative analysis of defects with the objective to identify critical defects.

* Corresponding author.

http://dx.doi.org/10.1016/j.matdes.2016.05.070
0264-1275/

Table 1
Optimization program.

Process parameter	Limits of variation or constant value
P — laser power [W]	100 ÷ 200
v — scanning velocity [mm/s]	200 ÷ 1100
h — hatch distance [μm]	40 ÷ 180
F — laser focus [mm]	−4, −3, −2, −1, 0, +1, +2, +3, +4, +5
δ — layer thickness [μm]	30
E_v — resulting energy density [J/mm^3]	50 ÷ 300
Strategy of laser scan	"cross" using zigzag scan vectors
Build platform heating [°C]	200

The total porosity is usually correlated to an average process energy applied per volume of material and described by energy density E_v as a ratio between laser power (P), scanning velocity (v), hatch distance (h) and layer thickness (δ) (see e.g. [5,6,22,34]):

$$E_v = \frac{P}{v \cdot \delta \cdot h}, \left[\mathrm{J/mm^3}\right] \quad (1)$$

Other approaches to quantify the energy introduced during the process include for example the line energy. However, using the volume energy is the most established approach today for continuous wave laser sources. Importantly, Eq. (1) does not represent the amount of energy actually introduced into the material: the effective volume energy, reduced by effects such as local and wavelength dependent absorption and reflectance properties of the power particles in the layer, the formed melt and plasma, is usually much lower [35,36]. Moreover, Eq. (1) does not take into account the energy introduced by subsequent passes of the laser as successive powder layers are deposited and melted. Nonetheless, E_v can be employed in many cases as a measure to analyze and adjust the process-materials relationships.

The objective of the present work is the investigation of the influence of SLM process parameters on the type and amount of porosity formed in TiAl6V4 aiming at obtaining a reliable process window for structural components. The porosity detection using 2D and 3D techniques is used for identifying the mechanisms of void formation, their topology and volume fraction as a function of energy density. Particular attention is paid to resolving the void morphologies at high resolution.

2. Material and experimental methods

2.1. TiAl6V4 powder

Powder of α-β titanium alloy TiAl6V4 (Ti — 6 wt% Al — 4 wt% V) provided by SLM Solutions was obtained by gas atomization in argon atmosphere resulting in spherical particles. The particle size distribution, measured by a particle size analyser (LS 13320 PIDS, Beckman Coulter), are obtained with the D-values 31 μm (D10), 42 μm (D50) and 53 μm (D90).

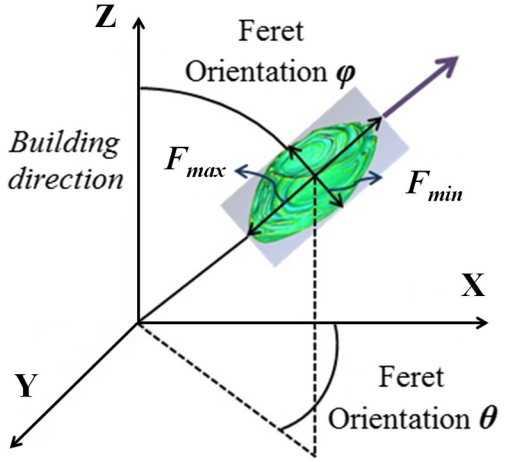

Fig. 1. 3D Feret orientations with respect to SLM building direction.

2.2. Optimization of SLM process

Cuboids of ~10 × 10 × 10 mm^3 were produced with various scan parameters (Table 1) by a SLM-250 Solution machine equipped with a 200 W laser of wavelength 1070 nm. The production of the samples was carried out in argon atmosphere and the temperature of the building platform was held at 200 °C. For this study, the temperature of the building platform was kept constant at this low temperature in order to suppress any phase transformation and microstructure dynamics due to the "external" heat source ("intrinsic" heat treatments due to laser patterns and absorbed laser energy dissipation unaffected).

For this study a one factor at a time (OFAT) approach was applied to identify straightforwardly the relative optima starting with a suitable parameter combination (175 W, 0.1 mm, 600 mm/s, focus 2) taken from previous studies [37].

2.3. Porosity analysis

The porosity of each cuboid sample was characterized qualitatively and quantitatively by 2D image analysis of metallographic longitudinal cross sections (parallel to the SLM building direction), and three-dimensionally by synchrotron tomography.

For 2D microstructural examination, the samples were first ground using a SiC grinding paper up to 4000 grit size, and polished using SiO_2–H_2O_2 slurry. The polished surfaces were etched in a mixture of 50 ml distilled water, 25 ml HNO_3 and 5 ml HF [38]. The microstructural study was performed on a ZEISS ULTRA 55 scanning electron microscope (SEM), while light optical microscopy (LOM) was carried out with a ZEISS LSM 700, which enabled imaging of large-area specimens due to the scanning workstation PILine and the stitching picture function of the imaging software ZEN 2012 (blue edition) [39]. The images were quantified using the software AnalySIS [40]. The investigated surface area was 10 × 10 mm^2 for each sample and 3 different parallel sections were evaluated for each parameter set. Each measured surface consisted of about 108 stitched pictures with a magnification of 100×

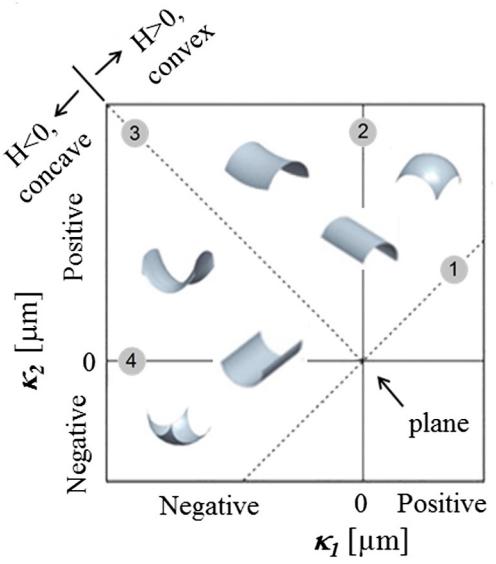

Fig. 2. Distribution plot of P (κ_1, κ_2), representing the probability of having a surface element with the curvature (κ_1, κ_2) and corresponding morphologies.
Adapted from [48].

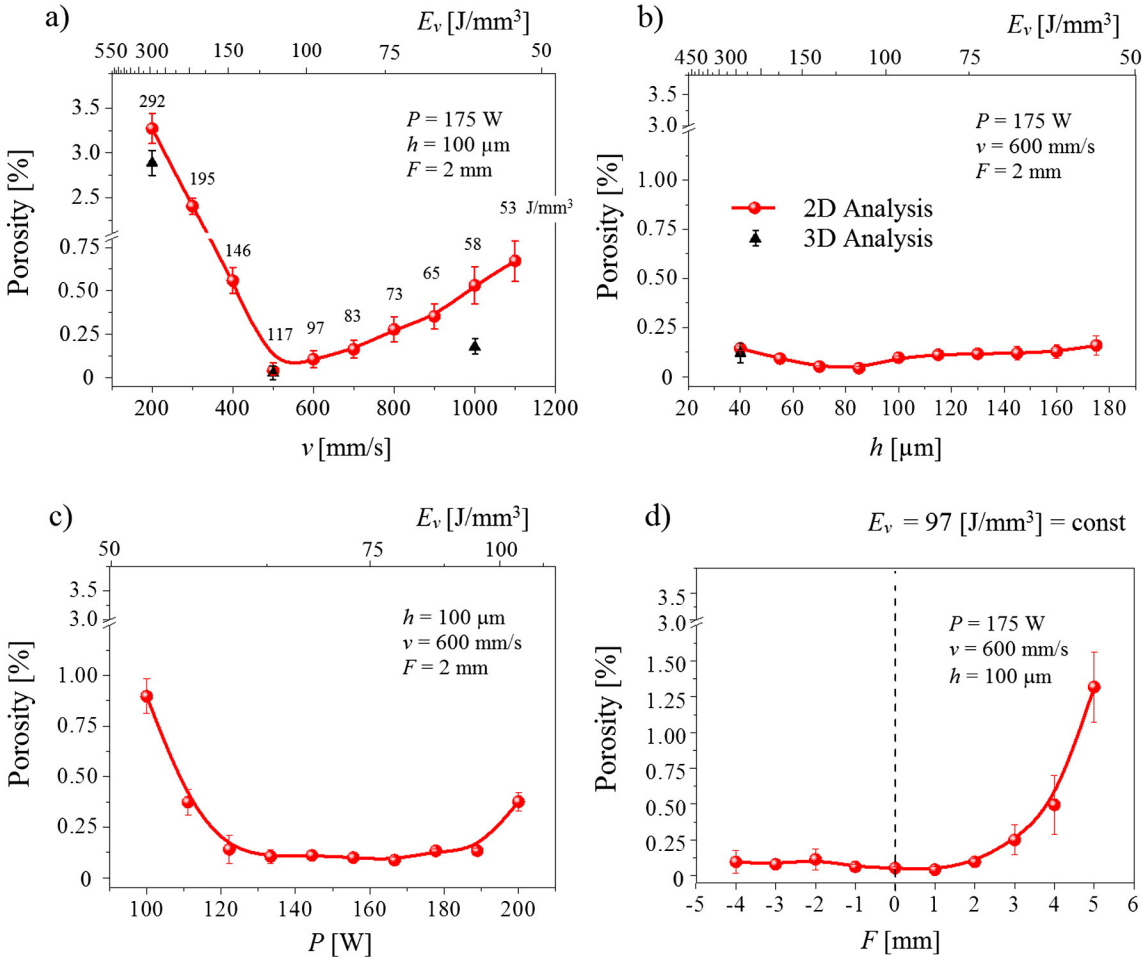

Fig. 3. Influence of the SLM process parameters on the total porosity (2D measurements) as a function of (a) scan velocity *v*, (b) hatch distance *h*, c) laser power *P* and (d) focus distance *F*. The volume energy density E_v, is included in the upper abscissae.

and 2584 × 1936 pixels. The circularity of the voids was calculated as:

$$C = \frac{4\pi \cdot A}{L^2}, \tag{2}$$

where *A* is the void area, *L* is the perimeter.

3D characterization of the voids was performed by synchrotron tomography at the ID19 beamline of the European Synchrotron Radiation Facility (ESRF), Grenoble, France. An energy of 35 keV was used for the tomographic scans. Cylindrical specimens with 0.8 mm diameter and ~7 mm length were extracted from SLM test cuboids. A total of 5969 radiographies were acquired between 0° and 180° using a pco.edge detector and an acquisition rate of 0.15 s/frame. An effective pixel size of $(0.33\ \mu m)^2$ and field of view of ~845 × 713 μm^2 were acquired for 3D

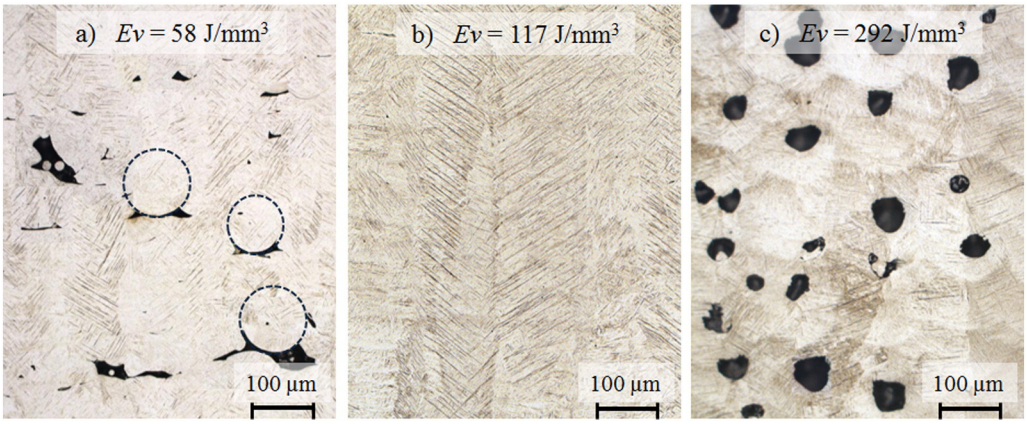

Fig. 4. 2D Pore morphologies obtained by LOM after SLM processing with different energy densities: (a) $E_v = 58\ J/mm^3 \ll E_{opt}$, (b) $E_{opt} = 117\ J/mm^3$ and (c) $E_v = 292\ J/mm^3 \gg E_{opt}$. The pores arising from low energy density (a) are induced among other effects by the balling effect and by unmolten particles (dashed circles). Some show satellite formation as evidenced by enclosed small spheres, which can be noted e.g. within the large pore on the left.

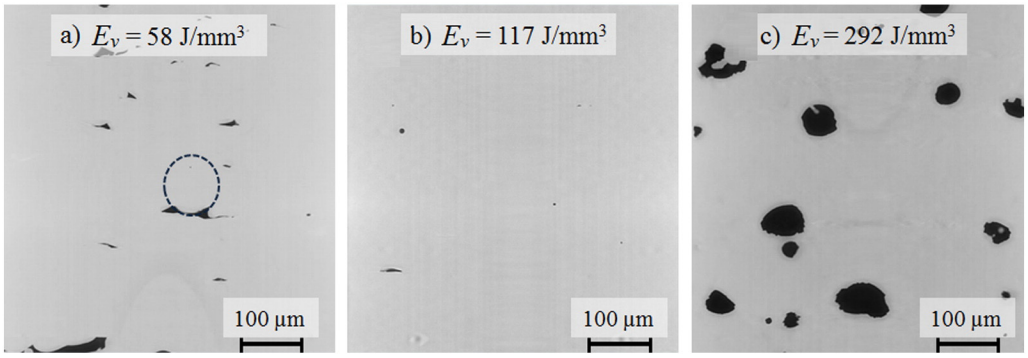

Fig. 5. 2D quantification of the voids area as a function of energy density E_v. Total number of voids versus their area classified within the 12 classes. Etched surfaces were analyzed.

reconstruction. The maximum measured volume was a cylinder with a diameter of 800 µm and length of 700 µm. The reconstructed volumes had a final size of Ø 2424 × 2121 voxels with a voxel size of $(0.33\ \mu m)^3$. Ring artefacts were filtered using a procedure described somewhere else [41]. Porosity segmentation was carried out by simple grey-value thresholding using the software FIJI [42]. 3D quantification was carried averaging the results for three specimens for each parameter set. Porosity morphology was analyzed using the software AVIZO Fire [43]. For each volumetric pore their area A, volume V, Feret parameters F_{min} and F_{max} as well as space orientation φ and θ as shown schematically in Fig. 1 were determined. Sphericity Ψ was calculated as:

$$\Psi = \frac{6 \cdot \pi^{\frac{1}{2}} \cdot V}{A^{\frac{3}{2}}} \tag{3}$$

Ψ is one for a sphere and becomes closer to zero for more concave, elongated or irregular shape of the voids.

The morphology of pores was analyzed by means of the local principal curvatures of pore surfaces. For this, principal radii of curvature r_1 and r_2 were determined, from which the two principal curvatures, $\kappa_1 = 1/r_1$ and $\kappa_2 = 1/r_2$, were obtained. First, a surface of the voxel-based volume was created from the segmented pores using the software AVIZO Fire [43]. The resulting surface is a triangular approximation of the segmented volumes. The curvatures were then calculated considering two direct neighbours to a certain triangle of the surface and the initial curvature values were smoothed by averaging them four times with the curvature values of direct neighbour triangles.

The local mean curvature H and the local Gaussian curvatures K are expressed as:

$$H = \frac{\kappa_1 + \kappa_2}{2} \tag{4}$$

$$K = \kappa_1 \cdot \kappa_2 \tag{5}$$

The pairs of principal curvatures $P\ (\kappa_1, \kappa_2)$ obtained in each studied region of the surface can be plotted as 2D dimensional contour diagrams, as shown in Fig. 2, to determine their morphology and relative occurrence [44–47]. By definition, the curvatures are selected such that $\kappa_2 \geq \kappa_1$, therefore, the distribution can have non-zero values only above the line $\kappa_2 = \kappa_1$. Other characteristic lines can be identified in the diagram [48]: (1) Points on the line $\kappa_2 = \kappa_1$ correspond to pore surface elements having locally a spherical topology which can be convex $(H > 0)$ or concave $(H < 0)$; (2) points along the line $\kappa_1 = 0$ $(\kappa_1 > 0)$ correspond to pore elements with a convex cylindrical topology; (3) along the line $\kappa_2 = \kappa_1$, the pore surface has a saddle shape with a zero mean curvature; and (4) along the line $\kappa_2 = 0$ $(\kappa_1 < 0)$, the pore surface element has also a cylindrical topology, but concave. The morphologies obtained in the regions enclosed by these lines are illustrated schematically in Fig. 2.

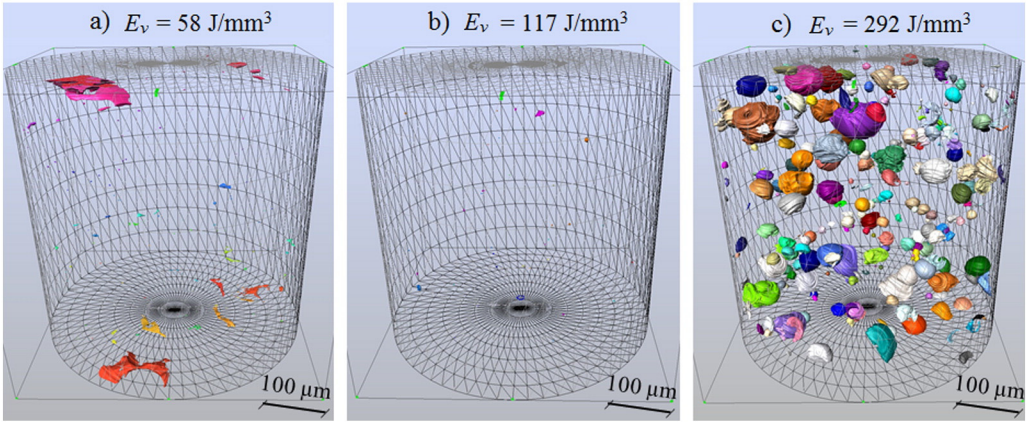

Fig. 6. 2D quantification of the voids shape factor (circularity) as a function of energy density E_v. Total number of voids versus shape factor classified within the 12 classes. Etched surfaces were analyzed.

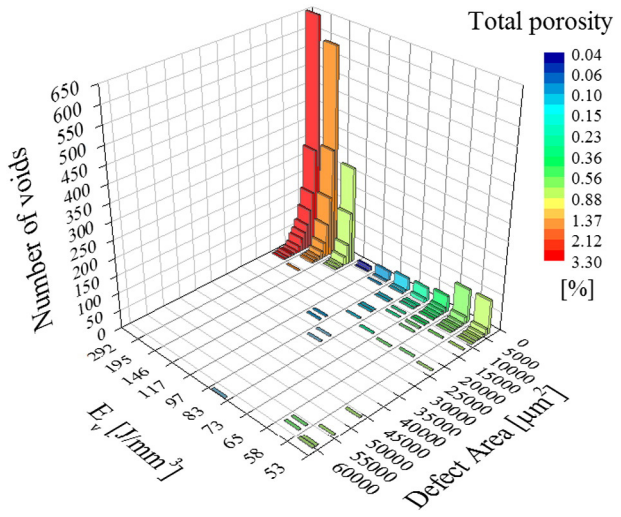

Fig. 7. Portions of synchrotron tomography slices showing the pore morphologies after SLM processing with different energy densities: (a) $E_v = 58$ J/mm$^3 \ll E_{opt}$, (b) $E_{opt} = 117$ J/mm^3 and (c) $E_v = 292$ J/mm$^3 \gg E_{opt}$. The pores arising from low energy density (a) induced among other by balling effect (dashed circle).

3. Results and discussion

3.1. Influence of the SLM process parameter on porosity

The variation series of the SLM process parameters *v*, *h*, *P* and *F* for the given cross-hatching scan strategy (with zigzag scan vectors) [5] and powder layer thickness (30 µm) showed that the velocity (all other parameters fixed; for details see experimental section) exerts the most dominant influence on the porosity fractions (Fig. 3). Besides the velocity (Fig. 3(a)), the laser power has significant influence on the resulting defect densities and also shows a distribution with an optimal parameter range allowing minimal defects (Fig. 3(c)). While the hatch distance was found to be least sensitive (Fig. 3 (b)), the focus only led to an increased fraction of voids when moved sizably downwards (positive focus range) below the powder bed surface (Fig. 3(d)). Thus, the robustness of the SLM process is mostly influenced by the choice of the velocity (and together with it also the scan strategy) and laser power, while it is least sensitive to the hatch distance.

The minimum porosity fraction in the velocity variation series (keeping power, hatch distance and focus constant) is at 0.042 ± 0.008% for 2D (and 0.028 ± 0.009 for 3D analysis) for $v = 500$ mm/s (Fig. 3 (a)). At lower velocities, a steep increase of the porosity to >3% is observed as the energy density introduced into the material becomes excessively large. Beyond velocities of 500 mm/s, E_v decreases quickly below 50 J/mm^3 and with it the global porosity of the samples rises very steadily up to >0.5% at 1000 mm/s, according to the 2D analysis. As mentioned above, the hatch distance affects overall porosity only minimally and can be considered the least sensitive parameter (within the boundaries chosen here; Fig. 3 (b)), i.e. the variation of the porosity stays below 0.1% at small (40 µm) or large hatch distances (180 µm). This is attributed to the fact that even at large hatch distances the melt pools are sufficiently large to overlap. On the other hand, small hatch distances lead to remelting, which does not significantly reduce the porosity at this low overall porosity level. However, considerable pore formation in the boundary regions of the SLM samples was detected towards small hatch distances below 60 µm (Fig. 15, supplementary material), which may arise by significant local overheating during the laser's return movement. Therefore, hatch distances lower than 60 µm cannot be recommended if a zigzag laser strategy is employed.

The laser power variation in the range from 100 to 200 W indicates a rather wide zone with reduced porosity fraction (Fig. 3 (c)). This optimal power window reaches from ca 122 to ca 190 W. The 2D-measured porosity stays below ~0.1%, whereas for lower and higher laser powers steep increases occur (to ~0.9 and ~0.4%, respectively). This shows that the impact of the parameter power should be considered essential, but the sufficiently wide window with low sensitivity to variations suggests that this parameter allows for a good robustness of the SLM process.

Finally, the effect of the laser focus (Fig. 3 (d)) shows a plateau region with low porosity <0.25% for focus values from −5 to 2 mm, which is followed by a steep increase to >1% for larger values moving the focal plane into the material. Hence, focus values larger than 2 mm cannot be recommended for the cross laser scan strategy with zigzag scan vectors.

Three SLM parameter sets were selected for a detailed 2D and 3D analysis of porosity, i.e. excessive overheating $E_v \gg E_{opt}$, $E_{opt} = 117$ J/mm^3 and insufficient energy $E_v \gg E_{opt}$, where E_{opt} was chosen considering the minimum porosity volume fraction as a function of scan velocity (Fig. 3 a)). The optimized energy E_{opt} obtained in this study is very close to optimum energy density of 120 J/mm^3 reported for pure Ti and Ti-Ti/B at a hatch distance of 100 µm and layer thickness of 100 µm by Attar et al. [11,14]. However, one must keep in mind that similar energy densities can be achieved by very different combinations of laser power, scanning velocity, hatch distance, scan strategy and layer thickness. Since the effects of the parameters do not behave strictly linearly and, e.g., a faster velocity cannot be simply offset by higher laser power or smaller layer thickness, a comparison by energy density only can be misleading.

At low energy densities $E_v \ll E_{opt}$, both defects due to insufficient melting and due to balling occur and lead to incomplete powder layer binding ("lack of fusion"). These binding defects form between layers and are aligned parallel to them (s. Fig. 4 (a): for the energy of 58 J/mm^3)): left over powder particles, only partially connected to the solidified alloy, exhibit complex, elongated and sharp crack-like voids and can be distinguished from balling defects (also not connected to lower layers) particularly by their grain structure: in the case of balling, the grain structure consists of lamellae of α′ martensite needles that show a continuous growth transition into the microstructure of the surrounding material. In case of unmolten particles, the microstructure varies more locally due to the particles original grain structure. In the 2D sections, they show widely-varying lengths between some 10 and >200 µm, the former being much smaller than the typical melt track width. These defects are typically considered critical for mechanical performance, especially if they are oriented horizontally to tensile load

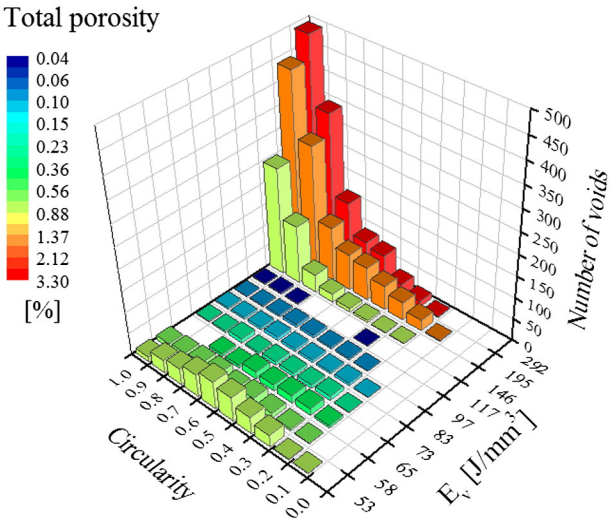

Fig. 8. 3D pore morphologies obtained by synchrotron tomography after SLM processing with different energy densities: (a) $E_v = 58$ J/mm$^3 \ll E_{opt}$, (b) $E_{opt} = 117$ J/mm^3 and (c) $E_v = 292$ J/mm$^3 \gg E_{opt}$. Cylindrical specimens with a diameter of 800 µm and height of 700 µm are presented. The TiAl6V4 matrix is transparent.

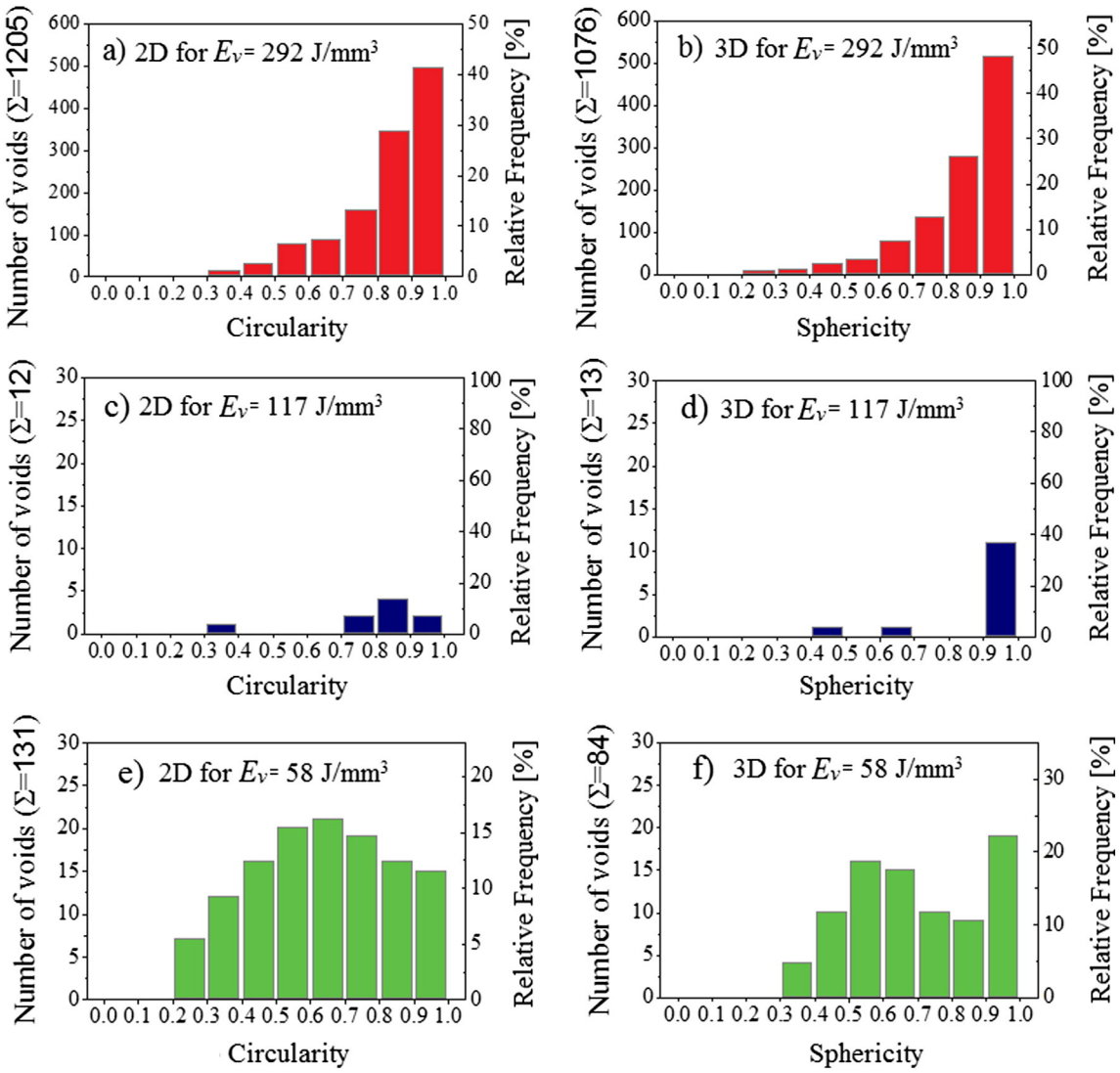

Fig. 9. Distribution of circularity (2D)/sphericity (3D) of pores for: (a, b) $E_v = 292$ J/mm$^3 \gg E_{opt}$, (c, d) $E_{opt} = 117$ J/mm^3 and (e, f) $E_v = 58$ J/mm$^3 \ll E_{opt}$.

direction [32,49–51]. Such defects reduce the effective load-bearing area perpendicular to the layers (building-direction) and cause stress concentrations (notch effect), resulting in reduction of static and dynamic strength in building-direction [51]. The sharper rims and crack tips are mostly affected by the balling phenomenon, which is the break-up of the melt pool into small spheres. This occurs when molten material does not wet the underlying substrate well due to high surface tension differences generated as a result of variations in thermal properties across the melt pool [52–54]. Thermal gradients can cause a thermocapillary flow of a fluid within the melt pool from regions with low surface tension to regions with high surface tension; this is known as Marangoni convection [55]. The breaking up of the melt pool into smaller entities reduces the variation in melt pool surface tension. Balling can increase with the generation of excessive molten material or if viscosity within a melt pool is too low [56]. Kruth et al. [53] stated that balling takes place when the total surface of a molten pool becomes larger than that of a sphere with the same volume.

The total porosity, as obtained at the insufficient energy density, can also be increased due to partially melted, entrapped powder particles that stick to and agglomerate on the outer edge of the solidified melt pool. This is known as "satellite formation" or "hillocks" [57,58]. Satellite formation mainly occurs when powder particles are not given enough time or heat to penetrate the melt pool before melt pool solidification [31].The particles, which did not melt completely, are pulled into the melt pool. As a result, after cooling the melt, a sphere-like body appears and its surface is covered by "hillocks" of individual particles [57].

At the opposite of the energy range (292 J/mm^3), round pores are generated in the SLM process (Fig. 4 (c)), which have been attributed in other studies to (i) inert gas entrapment [22] (ii) inert gas dissolved in liquid melt and released on solidification [22] and (iii) metal gas evaporated by high laser energies and resolidification [34,59]. Many researchers have attributed this phenomenon to the so-called keyhole effect [among others: [14,60,61]], although a definitive experiment revealing whether gas is entrapped in the pores has as of yet not be reported. While few have diameters around 10 μm in the 2D investigations, most are quite large with >100 μm. These pores are not perfectly circular, i.e. already the 2D analysis with light microcopy shows that they possess irregular perimeters, which will be discussed further in the 3D tomography characterization of this SLM condition.

Finally, at medium energies densities of 117 J/mm^3 (E_{opt}), an almost pore-free microstructure is observed (Fig. 4 (b)). It is worth noting that a few very small defects can still be recognized in the upper left hand corner of the image: a small pore of ca. 1 μm diameter and a very narrow crack (the sizes may be affected slightly by sample polishing and etching). While the tiny round defect may not be crucial [32], avoiding cracks even at the cost of an increased content of spherical porosity at slightly higher energies may be a desirable strategy. All these types of

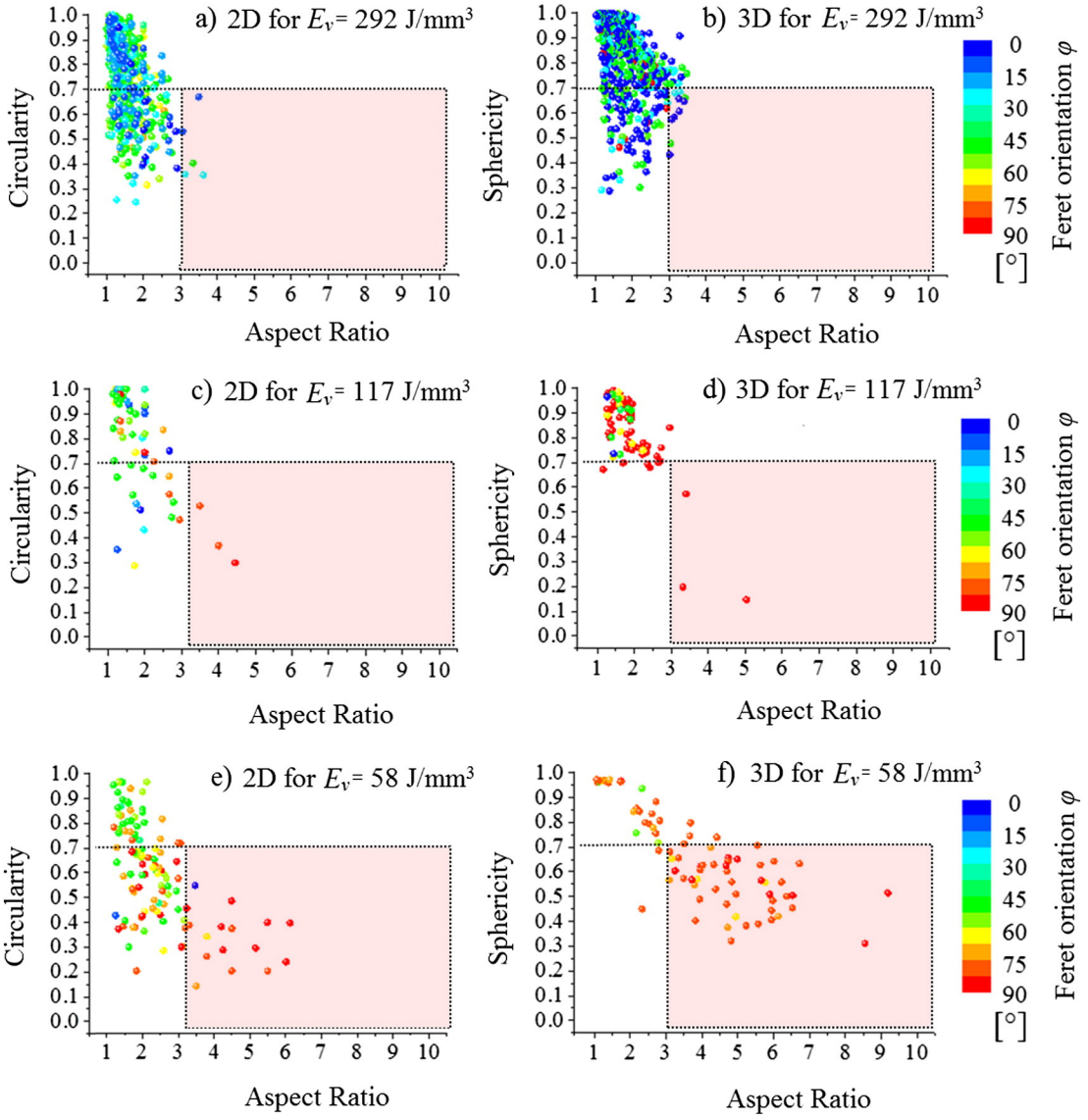

Fig. 10. Correspondence between circularity (2D)/sphericity (3D) of pores for: (a, b) $E_v = 292$ J/mm³ $\gg E_{opt}$, (c,d) $E_{opt} = 117$ J/mm³ and (e, f) $E_v = 58$ J/mm³ $\ll E_{opt}$.

the defects have also been described in investigations that employed e.g. micro-sectioning with LOM or SEM or micro-CT [22,33,34,62,63].

3.2. 2D quantitative analysis

A statistical analysis of the defects identified in the LOM images can be employed to characterize the defects by size and shape descriptors. For this, the (sectioned) voids area and shape factor are shown together with the number of voids in Fig. 5 and Fig. 6, respectively. Binning the total number of voids within 12 classes, it becomes evident that the vast majority of pores at large E_v ($E_v \gg 117$ J/mm³) have dimensions below 10,000 μm². These are the round melt pores formed due to excessive energy introduction into the material. The analysis of the circularity of the defects on the LOM images evidences that their shape is on average more roundish than that at lower energy densities (Fig. 6, circularities distributed largely towards 1 for $E_v \gg 117$ J/mm³).

The amount of small defects decreases significantly when the energy density shifts from excessive to medium energies (Fig. 5). With the further decrease of the energy density, the total amount of porosity gradually increases again due to the appearance of large linear defects with areas up to 60,000 μm². The shape analysis indicates a larger deviation from ideally spherical shapes for $E_v \gg 117$ J/mm³ (Fig. 6). Generally, the individual pore size grows dramatically between ~150 J/mm³ and ~100 J/mm³ with the occurrence of crack-like binding defects (Fig. 4), underlining that energy densities slightly lower than an optimal window in terms of porosity content are more critical than those at slightly higher values. In the optimal SLM energy density range, both high and low circularities are observed (Fig. 6) but, as discussed, at very low numbers. These results are qualitatively in agreement with the work published by Gong [33,34].

3.3. 3D porosity analysis

Characteristic regions of reconstructed synchrotron tomography slices are shown in Fig. 7 for the same SLM process conditions presented in Fig. 4. The different pore morphologies are clearly resolved by this technique. Rendered volumes of the pores present in these conditions are shown in Fig. 8 revealing their actual 3D morphology. Although irregular flat voids with sharp edges are not observed for high E_v, the morphology of the round pores (Fig. 8 (c)) is not as smooth as it may be inferred from the 2D-analysis (Fig. 4 (c)) or from micro-CT with its generally lower resolution [32].

The absolute 3D porosity fraction obtained from tomography analysis is very close to those measured by 2D analysis (Fig. 3).

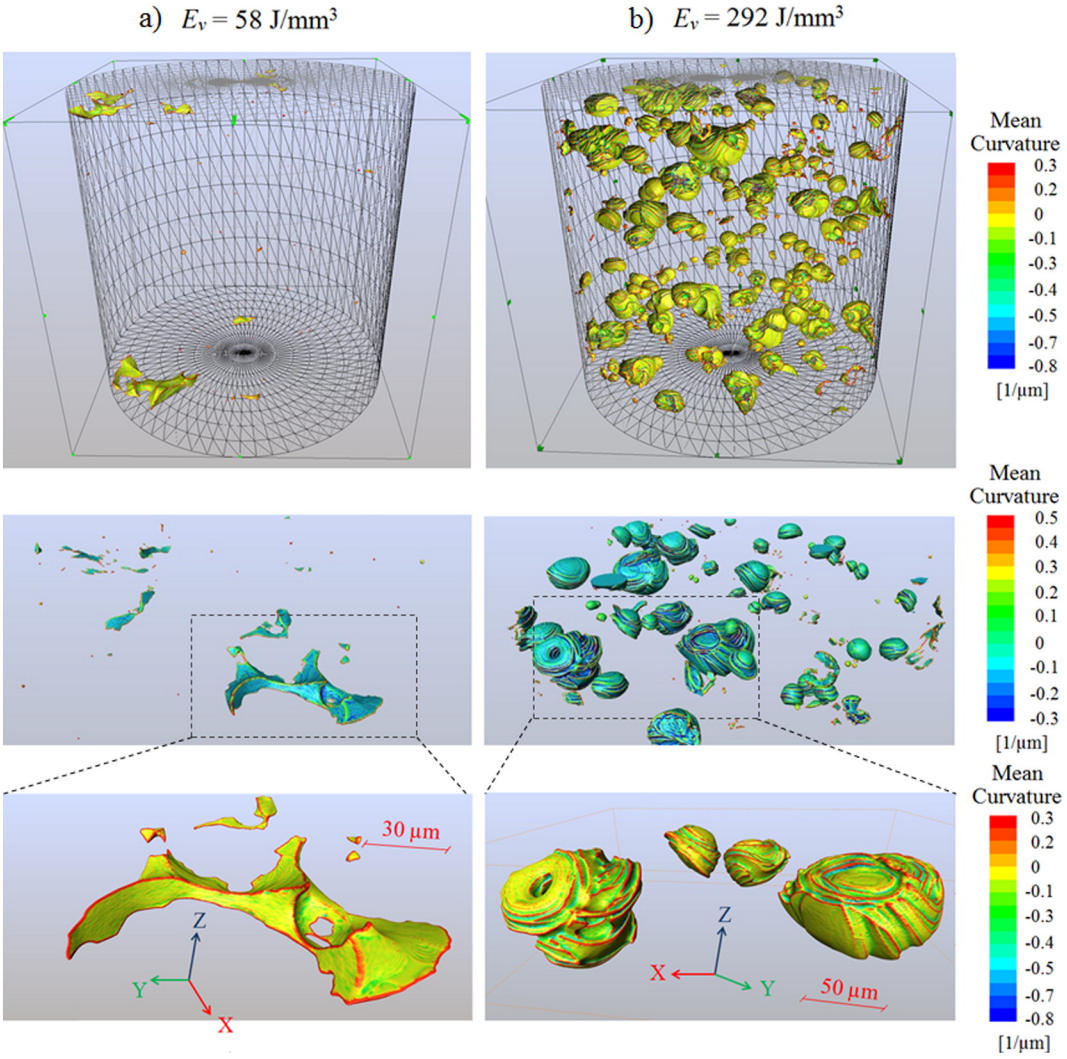

Fig. 11. Typical 3D mean curvatures of different void types: (a) $E_v = 58$ J/mm³, (b) $E_v = 292$ J/mm³. The size of bounding cylinders on the top: ø = 800 µm and h = 700 µm. The measured bounding boxes in the center have a size of 350 × 250 × 100 µm³. The TiAl6V4 matrix is transparent. The colour scale is the mean curvature.

Sphericity shows generally the same trend as circularity for the three chosen SLM energy densities although some differences can be observed (Fig. 9). The more irregular shape revealed in the 3D analysis for $E_v = 292$ J/mm³ (Fig. 8(c)) results in a broadening of the distribution towards lower sphericity values compared to the 2D analysis (Fig. 9 (a) and (b)). The histogram for the medium energy density shows the presence of irregular pores both in 3D and 2D, while a relative large amount of round pores are only revealed by the tomographic analysis (Fig. 9 (c) and (d)). Most of the pores resulting from the low heat flux ($E_v = 58$ J/mm³) have shape factors between 0.4 and 0.8 (Fig. 9 (e) and (f)).

The 3D data allows further insights for a first assessment of the expected materials' mechanical performance by correlating the aspect ratio with the voids shape and their orientation with respect to the building direction, which allows identifying the number of critical sharp defects (Fig. 10). The aspect ratio is calculated as the ratio between Feret parameters F_{max}/F_{min} both in the 2D and 3D analysis. Round pores, considered as those with circularity/sphericity >0.7, for which the aspect ratio hardly varies with respect to the specimen

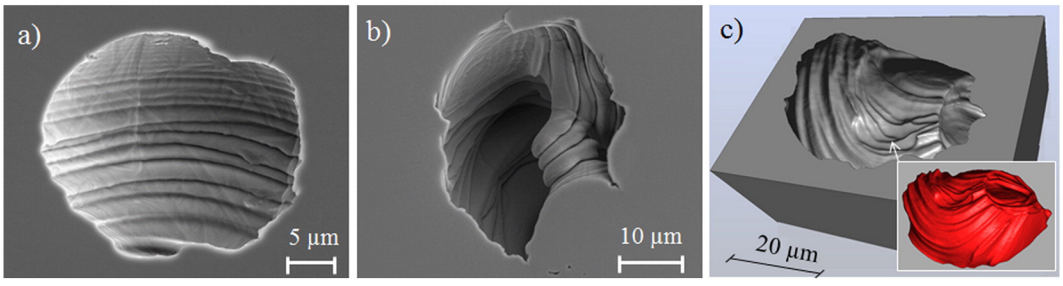

Fig. 12. 2D SEM images of pores (a, b) formed by excessive energy input: pore laid open by grinding reveals the same sharp rims found in the 3D tomography image (c). The rims/crinkles can be explained by the fact that during the highly dynamic SLM process the flowing melt is solidified abruptly.

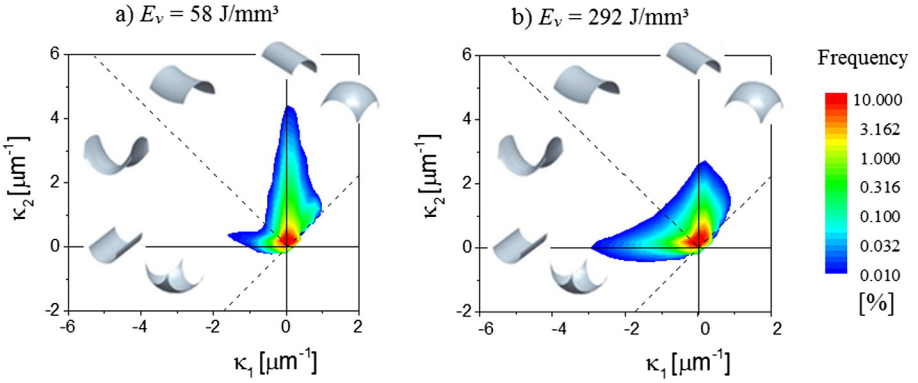

Fig. 13. Distribution of principal curvatures of the surface of pores: (a) $E_v = 58$ J/mm^3, (b) $E_v = 292$ J/mm^3. The colour scale is the normalised frequency.

build direction. The role of these pores on the alloy's mechanical behaviour is expected to be independent of the load direction. Crack-like voids, i.e. circularity or sphericity lower than 0.7 and large aspect ratio, can be critical from a mechanical point of view if they are oriented perpendicularly to the load direction [32,50]. These particularly critically oriented defects can be clearly identified by tomography and make up for the majority of non-spherical voids at the low energy density (Fig. 10 (e) and (f)). While 2D analysis underestimates the aspect ratio of these pores, it is the 3D tomography that enables to correctly characterize most of them to be truly orientated parallel to the powder layers.

The irregularity in the morphology of pores analysed in 3D by means of principal curvatures (Fig. 11) indicates sharp features lining the pore perimeters at small length scales. Here, the marginal energy density parameters are presented. Already a judgement by eyesight reveals that the pores formed at excessive energy densities (Fig. 11 (b)) possess sharp trenches that may act as stress concentrators as shown in Fig. 12 for the 2D and 3D images of the typical circular/spherical pores induced by $E_v \gg E_{opt}$. This rippling effect in the circular (spherical) pores occurs due to surface tension forces exerting a shear force on the liquid surface. Mumtaz and Hopkinson [31] explained it based on a (surface) temperature difference between the laser beam and the solidifying zone caused by the motion of the laser beam. As the thermal gradients reduce, gravity and surface curvature counteract the external shear force and eventually restores the surface height of the melt pool to the free level [64]. However, viscous forces delay this relaxation process and quick melt pool solidification often ensures that complete relaxation is not fully achieved.

The elongated defects resulting from insufficient energy ($E_v \ll E_{opt}$) exhibit even sharper rims and crack tips (Fig. 11 (a) for the energy of 58 J/mm^3), which can be affected among others by balling effect.

The principal curvature distributions for energy densities 58 and 292 J/mm^3 are shown in Fig. 13. The lower energy density (Fig. 13(a)) induces predominantly cylindrical shapes, consistent with elongated, binding failure defects, mostly with convex (along the vertical line)

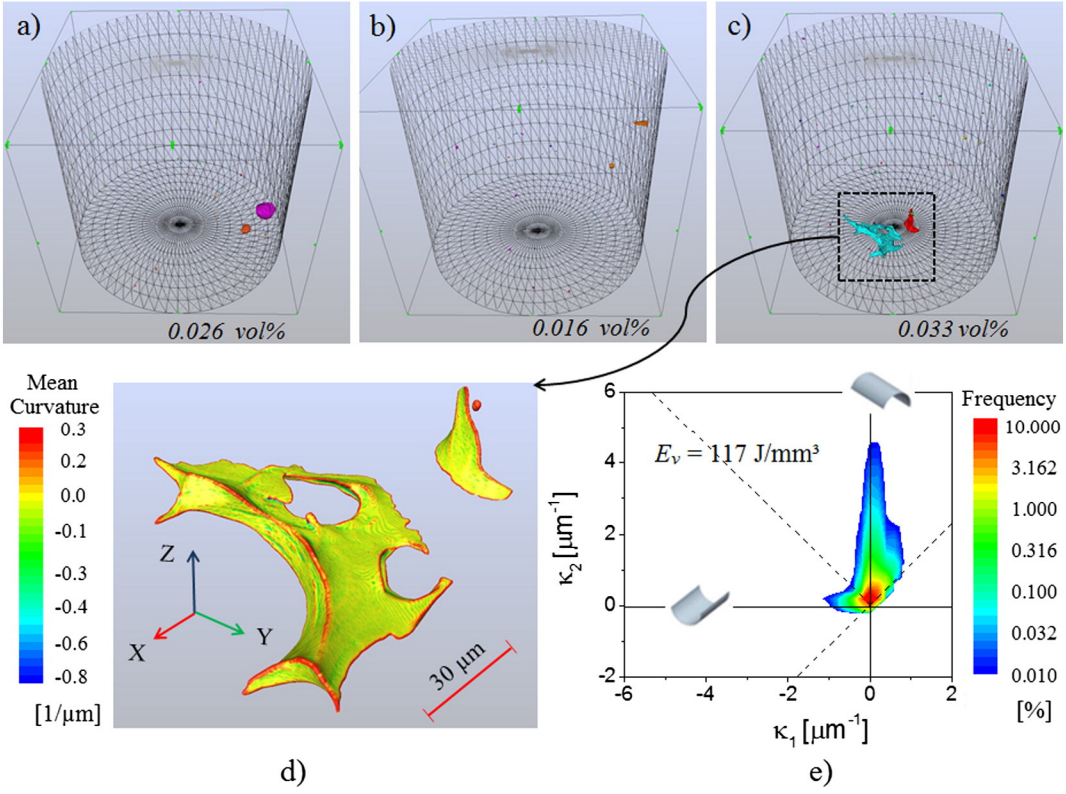

Fig. 14. (a–c): Typical voids obtained at optimized energy density E_{opt}. The size of the bounding cylinders is ø = 800 µm and h = 700 µm. (d): Detail of the flat crack-like void of Fig. 14 (c) with colour-coded mean curvature. (e): Distribution of principal curvatures of the surface of the void shown in Fig. 14 (d).

and some concave (along the horizontal line) surfaces. In contrast, the higher energy density results in the formation of pores with convex spherical and convex saddle surfaces.

As discussed above, the number of defects formed at the optimized energy density window is considerably the lowest, although both types of defects were detected in individual volumes (Fig. 14 (a) and (c)). These three volumes of the condition $E_{opt} = 117$ J/mm^3 demonstrate the presence of both spherical and elongated pores at low total porosity volume fractions. The flat crack-like defects (Fig. 14 (d)) show again the same morphology distribution (κ_1, κ_2) as the binding defects at lower energy densities (compare Fig. 13 (a) and Fig. 14 (e)) and are, therefore, expected to result in high stress concentration at the defect tips. Despite the achievement of a low porosity volume fraction, these residual binding defects cannot be avoided completely at the stage of power-layer consolidation at these optimized process parameters. The risk of such pore formation may either reduced by going to slightly higher energy densities at the risk of accepting a slight increase of spherical porosity. Their removal may also be largely possible by subsequent processing by thermomechanical treatment [33,37].

4. Conclusions

A systematic optimization strategy for the processing via selecting laser melting of Ti6Al4V was implemented aiming at obtaining a minimum porosity volume fraction. The correlation between processing parameters and void formation was determined combining 2D and 3D metallographic methods. The results lead to the following conclusions:

- The porosity of SLM parts can be significantly reduced with well optimized process parameters. A residual porosity of <0.05 vol% was achieved.
- At excessive or insufficient energy densities two major types of void defects are observed:
- Excessive energy density: circular/spherical pores with diameter of >50 μm induced probably by the keyhole effect. Their fine ribbed surface occurs due to surface tension forces exerting a shear force on the liquid surface.
- Insufficient energy density: elongated, narrow crack-like voids oriented preferably perpendicularly to the building direction. These voids can have lengths >100 μm. These pores are a result of binding faults (lack of fusion), mainly owing to incomplete melting of the metallic powders but also by the balling effect.

The SLM samples fabricated at intermediate energy densities show the lowest porosity volume fraction but scarce voids of both types, i.e. binding faults as well as round pores, were found. Therefore, energy densities slightly higher than that for which minimum volume fraction of porosity is obtained are recommended to avoid the presence of flat crack-like voids that can be detrimental for the mechanical performance of the alloy, particularly under fatigue conditions.

Supplementary data to this article can be found online at http://dx.doi.org/10.1016/j.matdes.2016.05.070.

Acknowledgements

The authors gratefully acknowledge Mrs. Elodie Boller for the support during the beam time at the ID19 beamline at the European Synchrotron Radiation Facility (ESRF), Grenoble, in the framework of project IN619. Mr. Tarik Merzouk is acknowledged for the SLM process support.

References

[1] F. Abe, K. Osakada, M. Shiomi, K. Uematsu, M. Matsumoto, The manufacturing of hard tools from metallic powders by selective laser melting, J. Mater. Process. Technol. 111 (1–3) (2001) 210–213.
[2] J.P. Kruth, G. Levy, F. Klocke, T.H.C. Childs, Consolidation phenomena in laser and powder-bed based layered manufacturing, CIRP Ann. Manuf. Technol. 56 (2007) 730–759.
[3] D.D. Gu, W. Meiners, K. Wissenbach, R. Poprawe, Laser additive manufacturing of metallic components: materials, processes and mechanisms, Int. Mater. Rev. 57 (2012) 133–164.
[4] B. Vrancken, L. Thijs, J.P. Kruth, J.V. Humbeeck, Microstructure and mechanical properties of a novel β titanium metallic composite by selective laser melting, Acta Mater. 68 (2014) 150–158.
[5] L. Thijs, F. Verhaeghe, T. Craeghs, J. Van Humbeeck, J.P. Kruth, A study of the micro structural evolution during selective laser melting of Ti–6Al–4V, Acta Mater. 58 (2010) 3303–3312.
[6] B. Vrancken, L. Thijs, J.P. Kruth, J.V. Humbeeck, Heat treatment of Ti6Al4V produced by selective laser melting: microstructure and mechanical properties, J. Alloys Compd. 541 (0) (2012) 177–185.
[7] C. Leyens, M. Peters, Titanium and Titanium Alloys: Fundamentals and Applications, Wiley-VCH, Weinheim, 2003.
[8] E.C. Santos, M. Shiomi, K. Osakada, T. Laoui, Rapid manufacturing of metal components by laser forming, Int. J. Mach. Tools Manuf. 46 (10) (2006) 1459–1468.
[9] K. Osakada, M. Shiomi, Flexible manufacturing of metallic products by selective laser melting of powder, Int. J. Mach. Tools Manuf. 46 (11) (2006) 1188–1193.
[10] D.D. Gu, Y.C. Hagedorn, W. Meiners, G.B. Meng, R.J.S. Batista, K. Wissenbach, R. Poprawe, Densification behavior, microstructure evolution, and wear performance of selective laser melting processed commercially pure titanium, Acta Mater. 60 (2012) 3849–3860.
[11] H. Attar, M. Calin, L.C. Zhang, S. Scudino, J. Eckert, Manufacture by selective laser melting and mechanical behavior of commercially pure titanium, Mater. Sci. Eng. A 593 (2014) 170–177.
[12] H. Attar, K.G. Prashanth, A.K. Chaubey, M. Calin, L.C. Zhang, S. Scudino, J. Eckert, Comparison of wear properties of commercially pure titanium prepared by selective laser melting and casting processes, Mater. Lett. 142 (2015) 38–41.
[13] L.C. Zhang, H. Attar, Selective laser melting of titanium alloys and titanium matrix composites for biomedical applications: a review, Adv. Eng. Mater. 18 (2016) 463–475.
[14] H. Attar, M. Bönisch, M. Calin, L.C. Zhang, S. Scudino, J. Eckert, Selective laser melting of in situ titanium–titanium boride composites: processing, microstructure and mechanical properties, Acta Mater. 76 (2014) 13–22.
[15] H. Attar, K.G. Prashanth, L.C. Zhang, M. Calin, I.V. Okulov, S. Scudino, C. Yang, J. Eckert, Effect of powder particle shape on the properties of in situ Ti–TiB composite materials produced by selective laser melting, J. Mater. Sci. Technol. 31 (2015) 1001–1005.
[16] E. Chlebus, B. Kuznicka, T. Kurzynowski, B. Dybala, Microstructure and mechanical behaviour of Ti–6Al–7Nb alloy produced by selective laser melting, Mater. Charact. 62 (2011) 488–495.
[17] T. Bormann, R. Schumacher, B. Müller, M. Mertmann, M. de Wild, Tailoring selective laser melting process parameters for NiTi implants, J. Mater. Eng. Perform. 21 (2012) (2519-2514).
[18] H. Meier, C. Haberland, J. Frenzel, R. Zarnetta, Selective Laser Melting of NiTi Shape Memory Components, Crc Press-Taylor and Francis Group, Boca Raton, 2010.
[19] L.C. Zhang, D. Klemm, J. Eckert, Y.L. Hao, T.B. Sercombe, Manufacture by selective laser melting and mechanical behavior of a biomedical Ti–24Nb–4Zr–8Sn alloy, Scr. Mater. 65 (2011) 21–24.
[20] S. Das, M. Wohlert, J. Beaman, D.L. Bourell, Processing of titanium net shapes by SLS/HIP, Mater. Des. 20 (1999) 115–121.
[21] L.E. Murr, S.A. Quinones, S.M. Gaytan, M.I. Lopez, A. Rodela, E.Y. Martinez, D.H. Hernandez, E. Martinez, F. Medina, R.B. Wicker, Microstructure and mechanical behavior of Ti–6Al–4V produced by rapid-layer manufacturing, for biomedical applications, J. Mech. Behav. Biomed. Mater. 2 (2009) 20–32.
[22] T. Vilaro, C. Colin, J.D. Bartout, As-fabricated and heat-treated microstructures of the Ti–6Al–4V alloy processed by selective laser melting, Metall. Mater. Trans. A 42A (10) (2011) 3190–3199.
[23] K. Puebla, L.E. Murr, S.M. Gaytan, E. Martinez, F. Medina, R.B. Wicker, Effect of melt scan rate on microstructure and macrostructure for electron beam melting of Ti–6Al–4V, Mater. Sci. Appl. 3 (2012) 259–264.
[24] H. Gong, K. Rafi, T. Starr, B. Stucker, The Effects of Processing Parameters on Defect Regularity in Ti–6Al–4V Parts Fabricated by Selective Laser Melting and Electron Beam Melting, 24th Annual International Solid Freeform Fabrication Symposium — An Additive Manufacturing Conference, Austin, TX, 2013 12–14.
[25] L. Facchini, E. Magalini, P. Robotti, A. Molinari, S. Hoges, K. Wissenbach, Ductility of a Ti–6Al–4V alloy produced by selective laser melting of prealloyed powders, Rapid Prototyp. J. 16 (2010) 450–459.
[26] T. Hua, C. Jing, Z. Fengying, L. Xin, H. Weidong, Microstructure and mechanical properties of laser solid formed Ti–6Al–4V from blended elemental powders, Rare Metal Mater. Eng. 38 (4) (2009) 574–578.
[27] D.D. Gu, Z.C. Hagedorn, W. Meiners, K. Wissenbach, R. Poprawe, Selective laser melting of in-situ TiC/Ti5Si3 composites with novel reinforcement architecture and elevated performance, Surf. Coat. Technol. 205 (2011) 3285.
[28] D.D. Gu, W. Meiners, Microstructure characteristics and formation mechanisms of in situ WC cemented carbide based hardmetals prepared by selective laser melting, Mater. Sci. Eng. A 527 (29–30) (2010) 7585–7759.
[29] R. Banerjee, D. Bhattacharyya, P.C. Collins, G.B. Viswanathan, H.L. Fraser, Precipitation of grain boundary α in a laser deposited compositionally graded Ti–8Al–xV alloy — an orientation microscopy study, Acta Mater. 52 (2) (2004) 377–385.
[30] R. Banerjee, P.C. Collins, A. Genc, H.L. Fraser, Direct laser deposition of in situ Ti–6Al–4V–TiB composites, Mater. Sci. Eng. A 358 (1) (2003) 343–349.
[31] K.A. Mumtaz, N. Hopkinson, Selective laser melting of thin wall parts using pulse shaping, J. Mater. Process. Technol. 210 (2010) 279–287.

[32] S. Leuders, M. Thöne, A. Riemer, T. Niendorf, T. Tröster, H.A. Richard, H.J. Maier, On the mechanical behaviour of titanium alloy TiAl6V4 manufactured by selective laser melting: fatigue resistance and crack growth performance, Int. J. Fatigue 48 (2013) 300–307.
[33] H. Gong, K. Rafi, N.V. Karthik, T. Starr, B. Stucker, Defect morphology in Ti–6Al–4V parts fabricated by selective laser melting and electron beam melting, Solid Freeform Fabrication Symposium Proceeding 2013, pp. 440–453.
[34] H. Gong, K. Rafi, H. Gu, T. Starr, B. Stucker, Analysis of defect generation in Ti–Al–4V parts made using powder bed fusion additive manufacturing processes, Addit. Manuf. 1 (2014) 87–98.
[35] N.K. Tolochko, Y.V. Khlopkov, S.E. Mozzharov, M.B. Ignatiev, T. Laoui, V.I. Titov, Absorptance of powder materials suitable for laser sintering, Rapid Prototyp. J. 6 (3) (2000) 155–161.
[36] J.P. Kruth, X. Wang, T. Laoui, L. Froyen, Lasers and materials in selective laser sintering, Assem. Autom. 23 (2003) 357–371.
[37] G. Kasperovich, J. Hausmann, Improvement of fatigue resistance and ductility of selective laser molten TiAl6V4, J. Mater. Process. Technol. 220 (2015) 202–214.
[38] G. Petzow, Metallographic Etching: Techniques for Metallography, Ceramography, Plastography, ASM International, Materials Park (OH), 1999.
[39] ZEN, SP1 (Black Edition)©, Carl Zeuss Microscopy GmbH, 2012 (1997-2013).
[40] AnalySIS©, Soft Imaging System GmbH, Muenster, Germany, 2002.
[41] M. Rodríguez Hortalá, G. Requena, B. Seiser, P. Degischer, M. Di Michiel, T. Buslaps, 3D-Characterization of continuous reinforced composites Proc. ICCM17 Int. Conf. on Composite Mat., Edinburgh 2009, pp. 1–9.
[42] (Fiji Is Just) — ImageJ© 1.49 s, Image Processing and Analysis in Java, Wayne Rasband, National Institute of Health, USA, 2010.
[43] AVIZO© Fire Edition 8.0.0., Visualisation Sciences Group, SAS, 1999-2013.
[44] R. Mendoza, J. Alkemper, P. Voorhees, The morphological evolution of dendritic microstructures during coarsening, Metall. Mater. Trans. A 34 (2003) 481–489.
[45] H. Meidani, J.L. Desbiolles, A. Jacot, M. Rappaz, Three-dimensional phase-field simulation of micropore formation during solidification: morphological analysis and pinching effect, Acta Mater. 60 (2012) 2518–2527.
[46] M. Felberbaum, M. Rappaz, Curvature of micropores in Al–Cu alloys: an X-ray tomography study, Acta Mater. 59 (2011) 6849–6860.
[47] H. Meidani, A. Jacot, Phase-field simulation of micropores constrained by the dendritic network during solidification, Acta Mater. 59 (2011) 3032–3040.
[48] D. Kammer, P.W. Voorhees, The morphological evolution of dendritic microstructures during coarsening, Acta Mater. 54 (2006) 1549–1558.
[49] P.A. Kobryn, S.L. Semiatin, Microstructure and texture evolution during solidification processing of Ti–6Al–4V, J. Mater. Process. Technol. 135 (2–3) (2003) 330–339 (2003).
[50] R. Cottam, M. Brandt, Laser cladding of Ti–6Al–4V powder on Ti–6Al–4V substrate: effect of laser cladding parameters on microstructure, Phys. Procedia 12 (2011) 323–329.
[51] I. Kelbassa. Qualifizieren des Laserstrahl-Auftragschweißens von BLISKs aus Nickel- und Titanbasislegierungen, Dissertation, RWTH Aachen, Germany, 2006.
[52] J.Y.H. Fuh, Y.S. Choo, A.Y.C. Nee, L. Lu, K. Lee, Improvement of the V curing process for the laser lithography technique, Mater. Des. 16 (1) (1995) 23–32.
[53] J.P. Kruth, L. Froyen, J. Van Vaerenbergh, P. Mercelis, M. Rombouts, B. Lauwers, Selective laser melting of iron-based powder, J. Mater. Process. Technol. 149 (1–3) (2004) 616–622.
[54] R. Morgan, C.J. Sutcliffe, W. O'Neill, Density analysis of direct metal laser remelted 316 L stainless steel cubic primitives, J. Mater. Sci. 39 (4) (2004) 1195–1205.
[55] M. Rombouts, J.P. Kruth, L. Froyen, P. Mercelis, Fundamentals of selective laser melting of alloyed steel powders, CIRP Ann. Manuf. Technol. 55 (1) (2006) 187–192.
[56] M. Agarwala, D. Bourell, J. Beaman, H. Marcus, J. Barlow, Direct selective laser sintering of metals, Rapid Prototyp. J. 1 (1) (1995) 26–36.
[57] N.K. Tolochko, S. Mozzharov, I.A. Yadroitsev, T. Laoui, L. Froyen, V.I. Titov, M.B. Ignatiev, Balling process during selective laser treatment of powders, Rapid Prototyp. J. 10 (2) (2004) 78–87.
[58] M.V. Elsen, Complexity of Selective Laser Melting: A New Optimization Approach. Phd. Department of Mechanical Engineering, Katholieke Universiteit Leuven, Leuven, 2007.
[59] X. Zhou, D. Wanga, X. Liu, D.D. Zhang, S. Qua, J. Ma, G. London, Z. Shen, W. Liu, 3D-imaging of selective laser melting defects in a Co–Cr–Mo alloy by synchrotron radiation micro-CT, Acta Mater. 98 (2015) 1–16.
[60] S. Pang, W. Chen, W. Wang, A quantitative model of keyhole instability induced porosity in laser welding of titanium alloy, Metall. Mater. Trans. A 45A (2014) (2808-2018).
[61] R. Rai, T.A. Palmer, J.W. Elmer, T. Debroy, Heat transfer and fluid flow during electron beam welding of 304 L stainless steel alloy, Appl. Phys. 88 (2009) 54–61.
[62] E. Brandl, Microstructural and Mechanical Properties of Additive Manufactured Titanium (Ti–6Al–4V) Using Wire: Evaluation With Respect to Additive Processes Using Powder and Aerospace Material Specifications, Aachen, Shaker Verlag, Germany, 2010.
[63] B. Baufeld, E. Brandl, O. van der Biest, Wire based additive layer manufacturing: comparison of microstructure and mechanical properties of Ti–6Al–4V components fabricated by laser-beam deposition and shaped metal deposition, J. Mater. Process. Technol. 211 (6) (2011) 1146–1158.
[64] J.A. Ramos, D.L. Bourell, J.J. Beaman, Surface over-melt during laser polishing of indirect-SLS metal parts, Mater. Res. Soc. (2003) 53–61 (Boston, MA, United States).

Materials and Design 112 (2016) 160–161

Contents lists available at ScienceDirect

Materials and Design

journal homepage: www.elsevier.com/locate/matdes

Corrigendum

Corrigendum to "Correlation between porosity and processing parameters in TiAl6V4 produced by selective laser melting" [Materials and Design 105 (2016) 160–170]

Galina Kasperovich *, Jan Haubrich, Joachim Gussone, Guillermo Requena

Institute of Materials Research, German Aerospace Center (DLR), Germany

The authors regret to inform that the some figures were reversed, namely the correct captions to the images 5–8 themselves were inserted incorrectly.

Author would like to apologize for the inconvenience caused.

Corrected numbering of the figures:

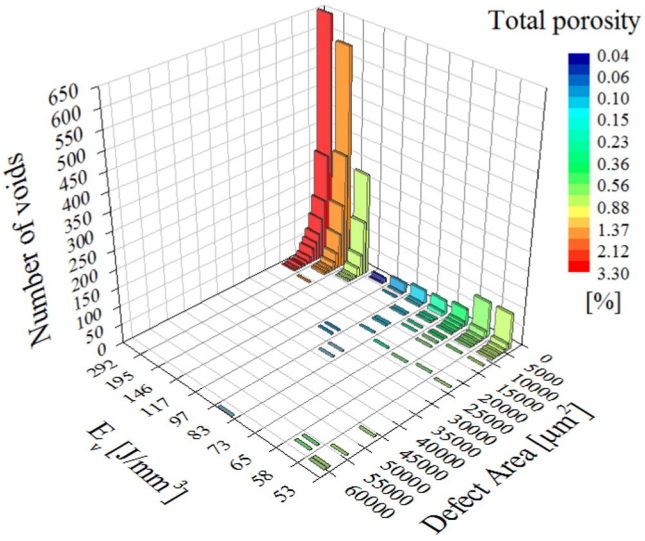

Fig. 5. 2D quantification of the voids area as a function of energy density *Ev*. Total number of voids versus their area classified within the 12 classes. Etched surfaces were analyzed.

DOI of original article: http://dx.doi.org/10.1016/j.matdes.2016.05.070.

* Corresponding author.
E-mail address: galina.kasperovich@dlr.de (G. Kasperovich).

http://dx.doi.org/10.1016/j.matdes.2016.09.040

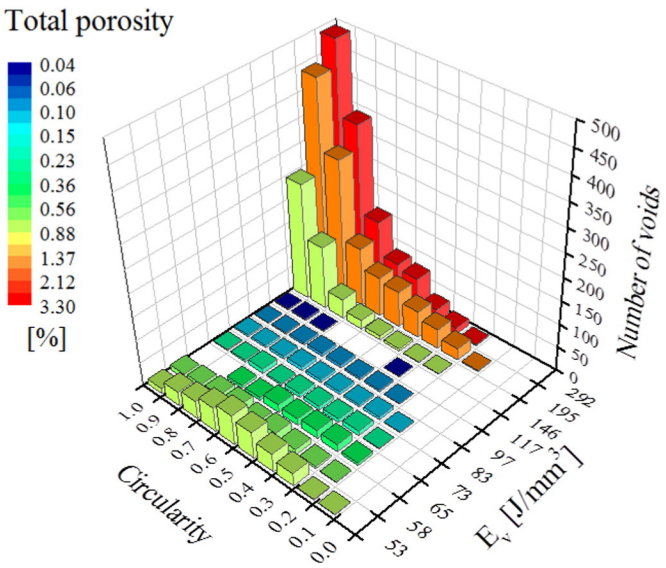

Fig. 6. 2D quantification of the voids shape factor (circularity) as a function of energy density *Ev*. Total number of voids versus shape factor classified within the 12 classes. Etched surfaces were analyzed.

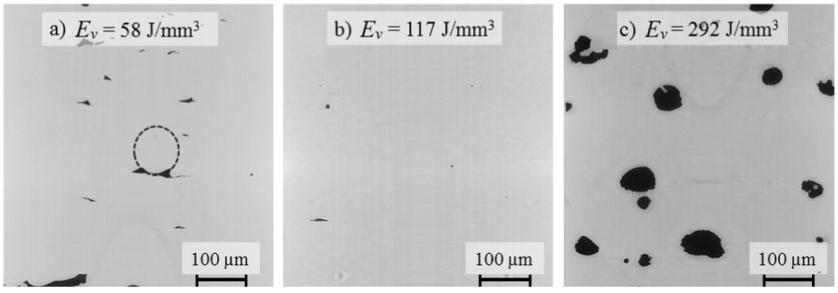

Fig. 7. Portions of synchrotron tomography slices showing the pore morphologies after SLM processing with different energy densities: (a) $E_v = 58$ J/mm^3 << E_{opt}, (b) $E_{opt} = 117$ J/mm^3 and (c) $E_v = 292$ J/mm^3 >> E_{opt}. The pores arising from low energy density (a) induced among other by balling effect (dashed circle).

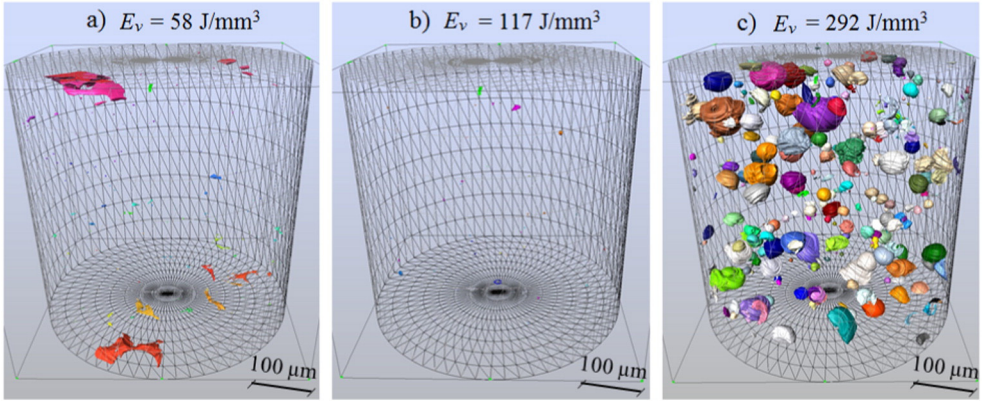

Fig. 8. 3D pore morphologies obtained by synchrotron tomography after SLM processing with different energy densities: (a) $E_v = 58$ J/mm^3 << E_{opt}, (b) $E_{opt} = 117$ J/mm^3 and (c) $E_v = 292$ J/mm^3 >> E_{opt}. Cylindrical specimens with a diameter of 800 µm and height of 700 µm are presented. The TiAl6V4 matrix is transparent.